RESEARCH ARTICLE | JULY 01 2026

Synthesis of chiral magnetic graphene nanoribbons on ferromagnetic $EuAu_2$

David Serrate ; Eliecer Peláez-Sifonte ; Fernando López-Tejeira ; Laura Fernández; Francisco Romero-Lara ; Katerina Vaxevani; Frederick Schiller

Low Temp. Phys. 52, 858–864 (2026)
https://doi.org/10.1063/10.0044342

Low Temperature Physics ARTICLE pubs.aip.org/aip/ltp

Synthesis of chiral magnetic graphene nanoribbons on ferromagnetic $EuAu_2$

Cite as: Fiz. Nizk. Temp. **52**, 952–959 (July 2026); doi: 10.1063/10.0044342
Submitted: 25 May 2026

David Serrate,[1,2,3,a)] Eliecer Peláez-Sifonte,[1] Fernando López-Tejeira,[3] Laura Fernández,[4] Francisco Romero-Lara,[5] Katerina Vaxevani,[5] and Frederick Schiller[4]

AFFILIATIONS

[1]Instituto de Nanociencia y Materiales de Aragón, CSIC-Universidad de Zaragoza, Zaragoza E–50009, Spain
[2]Laboratorio de Microscopias Avanzadas, Universidad de Zaragoza, Zaragoza E–500018, Spain
[3]Departamento de Física de la Materia Condensada, Universidad de Zaragoza, Zaragoza E–50018, Spain
[4]Centro de Física de Materiales (MPC) CSIC-UPV/EHU, San Sebastián E–20018, Spain
[5]CIC NanoGUNE-BRTA, E–20018, San Sebastián, Spain

[a)]**Author to whom correspondence should be addressed:** serrate@unizar.es

ABSTRACT

Low-dimensional carbon-based materials can show intrinsic magnetism associated with *p*-electrons. Besides, they can be fabricated with atomic precision by on-surface synthesis methods. This makes them appealing alternatives to overcome the limitations of traditional magnetic materials in fields like quantum devices or spintronics. A paramount example is graphene nanoribbons, which have been recently shown to display intrinsic extended magnetic ordering of their edge states [J. Brede, N. Merino-Díez, A. Berdonces-Layunta *et al.*, Nature Commun. **14**, 6677 (2023)] and to host spin moments with well-defined quantum states [A. Domínguez-Celorrio, L. Edens, S. Sanz *et al.*, Nature Commun. **16**, 5632 (2025)]. However, their spin state is determined by electron occupancy and spin exchange interactions, which can be tuned by the choice of a suitable substrate. In this work, we synthesize chiral graphene nanoribbons with a length of 3.5 nm on the monolayer alloy $EuAu_2$ grown on Au(111). By means of spin-resolved scanning tunneling microscopy and spectroscopy, we confirm the ferromagnetic state of the $EuAu_2$ and unveil the electron-doped charge state of the nanoribbons.

1. INTRODUCTION

Within the wide range of graphene nanostructures predicted to display π-magnetism,[1,2] graphene nanoribbons (GNRs) stand out in terms of potential applications due to their aspect ratio and length,[3,4] which facilitate integration into devices.[5,6] Graphene nanoribbons (GNR) can be manufactured with atomic-scale precision in their length, width, and edge geometry by means of on-surface synthesis (OSS) techniques.[7] Among them, zig-zag terminated longitudinal edges are expected to have the most robust magnetic ground state, stabilized by strong electron-electron correlations.[8,9] However, in this type of edge, the most stable resonant form is a multi-radical state, which makes it extremely reactive and difficult to synthesize.[1,10] Instead, chiral graphene nanoribbons with edges composed of periodic arrangements of zig-zag and armchair segments are substantially less challenging to synthesize and, at the same time, retain a non-zero spin in their edge states.[8,11–14]

Most of the OSS experiments leading to tailored nanographenes have been conducted on Au(111). In the case of GNRs, this surface is able to catalyze the Ullmann polymerization of the constituent precursors,[15] but induces a weakly charged cationic character, leaving the product GNRs in a closed-shell configuration in contrast with the neutral gas-phase state.[12] In order to restore the magnetic character of the GNRs, the electron occupancy of π-orbital states must be adjusted, as has been recently demonstrated on the MgO/Ag(001) surface.[14] GNRs have also been synthesized on various coinage-metal surfaces, but their surface reactivity is very different from that of Au(111), impeding the direct extrapolation of the extensive results obtained in that substrate. In the last few years, it has been shown that $REAu_2$ (rare earth, RE = Gd, Tb) monolayer alloys grown on Au(111) can support the same reactions as the bare Au(111) with minimal variations of the procedures. The choice of RE[13,16] and the various

surface reconstructions[17] of these alloys allow us to modulate in a controllable manner the local contact potential, and thus the degree of charge transfer from or to the GNRS. Furthermore, the ferromagnetic nature of the 2D overlayers[18–20] serves as an excellent tool to investigate the magnetism of GNRs. For instance, direct experimental proof of the stationary spin polarization was achieved by some of us using the exchange interaction between the $GdAu_2$ surface and the metallic edge states of the GNRs.[13] The localized counterpart of this scenario was also addressed in the form of the exchange splitting of singly occupied molecular orbitals confined to small regions comprising a few benzene rings. This is the case for small triangulenes on $TbAu_2$[21] and symmetry-protected topological end states (SPTES) of chiral GNRs on $GdAu_2$.[17]

Spin-polarized scanning tunnelling microscopy (SP-STM) of $GdAu_2$ evidences a strong easy-plane anisotropy,[13,18] which represents a significant drawback for most experimental set-ups featuring external magnetic fields that are applied normal to the surface. Moreover, its surface reconstruction is not commensurate with either the $GdAu_2$ nor the Au lattice, causing a large dispersion of the exchange field exerted by the surface on the GNRs.[13,17,21] On the other hand, $TbAu_2$ is a soft out-of-plane ferromagnet,[21] exhibits a commensurate reconstruction, and has proved to sustain the growth of armchair GNRs.[16] However, SP-STM data in this system remains elusive, and there is no information on the local spin arrangement of the Tb lattice. Successful OSS has not been reported to date in $REAu_2$ surfaces other than these two, and the influence of the RE element 4*f*-filling on the magnetic exchange and its single-ion anisotropy remains largely unexplored.

In this study, we investigate the magnetic and electronic properties of GNRs synthesized on the $EuAu_2$ 2D alloy. SP-STM reveals a ferromagnetic ground state of $EuAu_2$ with a marked out-of-plane easy axis. In contrast with other $REAu_2$ surfaces of the family, individually dispersed Eu adatoms on top of the perfect epitaxial reconstruction persist under any preparation conditions. They have a strong impact on the surface reactivity. Chiral GNRs can be synthesized, but the Eu adatoms severely hinder the formation of specimens longer than three precursor units (about 3.5 nm). The comparison with tight-binding calculations indicates that the GNRs have anionic character with a charge transfer of at least 0.5 e^-/nm.

2. EXPERIMENTAL AND THEORETICAL METHODS

Sample preparation. The Au(111) single crystal from Mateck GmbH was cleaned by repeated Argon sputtering and annealing processes at 510 °C. $EuAu_2$ alloy is grown on the clean Au(111) surface by sublimating Eu using an e-beam source at a rate of approximately 0.07 ML/min (Fig. 1(b) while the substrate is held

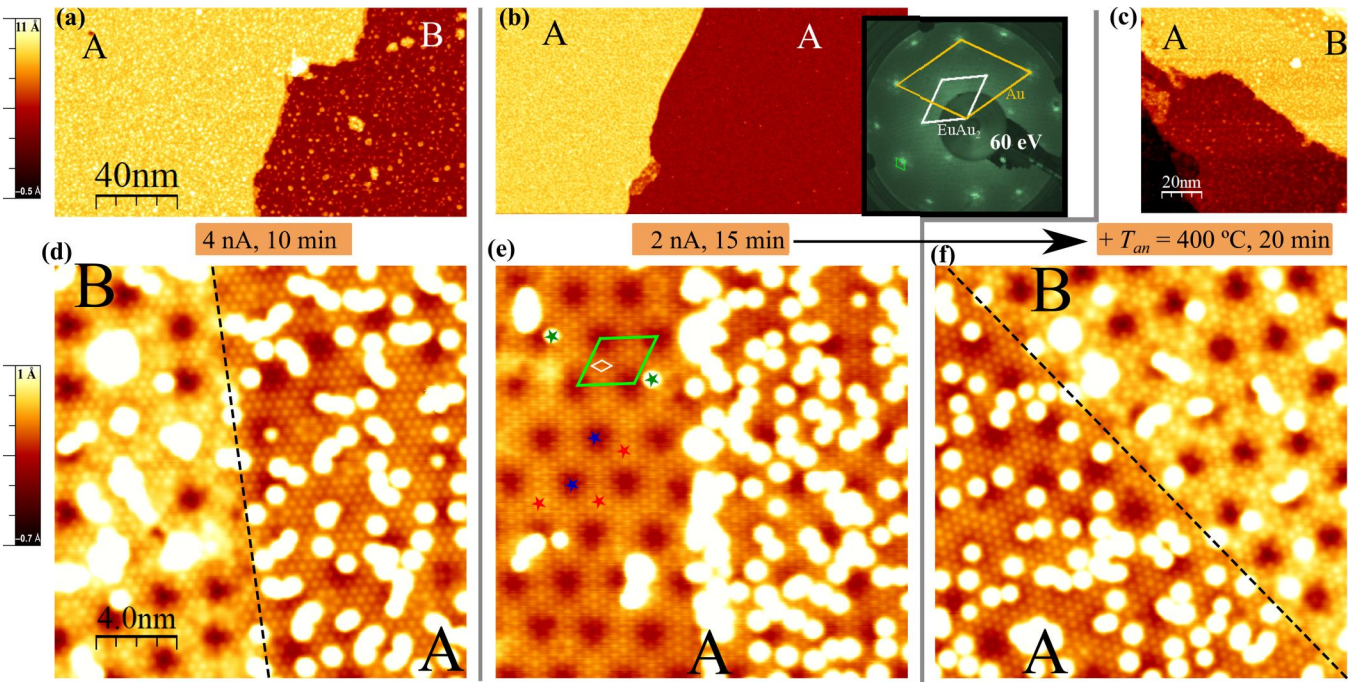

FIG. 1. Epitaxial growth of $EuAu_2$/Au(111). (a), (b) Large-scale surveys of the samples obtained after using two different deposition conditions (Eu flux and time indicated in the boxes) at a temperature T_s = 345 °C. Capital A and B letters indicate the regions where the two $EuAu_2$ phases exist (see text). In (b), the LEED micrograph was taken at a beam energy of 60 eV with the three unit cells depicted by polygons. (c) Survey of the sample in (b) after an additional postannealing of 20 min at T = 400 °C. (d), (e), (f) Close-ups of the same samples as in (a), (b), (c) with atomic resolution of both phases. Dashed lines mark the boundary between phases A and B. Bright saturated spots are the Eu adatoms in phase A or clusters in phase B. STM parameters: (a), (b) are taken at V_s/T_s =1 V/30 pA; (c) at – 0.5 V/30 pA; and (d), (e), (f) at 10 mV/1 nA. T = 1.1 K for (e) and T = 4.3 K for all the others.

at temperature T_s. The precursor (1) 2′,3″-dibromo–9,9′:10′,9″:10″,9‴-quarteranthracene, shown in Fig. 3(a), is then deposited on $EuAu_2$ from a home made resistive evaporator. Subsequent on-surface synthesis of (3,2,8)-GNRs is performed by stepwise annealing of this deposit, as illustrated by Fig. 3.

STS/STM measurements. All measurements have been performed at the SPECS-JT-STM of the Laboratory for Advanced Microscopy (University of Zaragoza), with a base temperature of 1.13 K and an out-of-plane magnetic field up to 3 T provided by a dry superconducting split-coil. The whole facility operates under ultra-high-vacuum conditions ($P \sim 1 \cdot 10^{-10}$ mbar). The tip is grounded, and the tunneling bias V_b is applied to the sample. Data has been taken at $T = 1.1$ or 4.3 K as stated in the captions. Differential tunneling conductance dI/dV is acquired using a lock-in amplifier at a frequency of 933 Hz and root-mean-square (r.m.s) modulation given by V_{mod}. STM images and dI/dV maps were taken in constant current mode, using a regulation distance determined by the set point V_s/I_s indicated at the corresponding caption for each data set. Spin-polarized STM (SP-STM) has been carried out using bulk Cr tips with out-of-plane sensitivity. Tips were prepared by electrochemical etching of elongated pure Cr wires of 1 mm diameter, and subsequent field emission cleaning (120 V, 1 μA, 1 h) at the STM head.

Tight Binding calculations. To theoretically describe GNRs, we employ the following tight-binding (TB) Hamiltonian,[22] with the on-site Coulomb repulsion parameter U set to zero

$$H = -t_1 \sum_{\langle i,j\rangle,\sigma} c^{\dagger}_{i\sigma} c_{j\sigma} - t_2 \sum_{\langle\langle i,j\rangle\rangle,\sigma} c^{\dagger}_{i\sigma} c_{j\sigma} - t_3 \sum_{\langle\langle\langle i,j\rangle\rangle\rangle,\sigma} c^{\dagger}_{i\sigma} c_{j\sigma}, \quad (1)$$

where $\sigma = \{\uparrow, \downarrow\}$ are the two spin components and $t_{1,2,3}$ are the hopping terms corresponding to the interaction between first, second, and third nearest neighbors (3NN), respectively. We use the parametrization of Ref. 12 with numerical values $t_1 = 2.7$, $t_2 = 0.2$, $t_3 = 0.18$ eV, corresponding to neighbour distances comprehended between $d_1 < 1.6$ Å $< d_2 < 2.6$ Å < 2.6 Å $< d_3 < 3.1$ Å, respectively. Numerically, we solve the Schrödinger equation, Eq. (1), using the Python package Hubbard from Refs. 23 and 24.

We obtain the local density of states (LDOS) simulated images as done in Ref. 13,

$$\mathrm{LDOS}(\mathbf{r}, E) = \sum_n \mathrm{LDOS}_n(\mathbf{r}) \frac{\gamma/\pi}{(E - E_n)^2 + \gamma^2}, \quad (2)$$

where

$$\mathrm{LDOS}_n(\mathbf{r}) = \sum_{\sigma} \left| \sum_i b_{ni\sigma} \phi(\mathbf{r} - \mathbf{R}_i) \right|^2 \quad (3)$$

and $b_{\sigma ni}$ is the projection on the $2p_z$-orbital located at site i of eigen-state number n and spin orientation σ at energy $E_{n\sigma}$. $\phi(\mathbf{r} - \mathbf{R}_i)$, centred at position $\mathbf{R}_i$, is described by the radial function $\exp(-3|\mathbf{r} - \mathbf{R}_i|/\text{Å})$, and represents the carbon $2p_z$ basis orbital.

The Lorentzian broadening around each eigen-energy is set to $\gamma = 10$ meV in simulated images, in order to take into account the mixing of energetically closely-spaced orbitals. We slice the grid at a height of $z = 25$ Å above the GNR. We plot these quantities using the Hubbard Python package from Ref. 23.

3. FERROMAGNETIC $EuAu_2$ MONOLAYER

We first start by optimizing $T_s = 345\,^{\circ}C$ to form a single crystalline $EuAu_2$ monolayer (ML). Figure 1(b) shows an STM overview representative of this process for 1 ML coverage. The corresponding LEED pattern exhibits the well-known $\sqrt{3} \times \sqrt{3}R30$ $EuAu_2$ unit cell relative to the Au lattice in the alloy, where each Eu atom is surrounded by 6 Au atoms.[20] A longer range 9×9 reconstruction (marked in green) relative to the Au lattice is also visible (therefore, 30° rotated with respect to the Eu lattice). In STM images, this reconstruction typically gives rise to a pronounced hexagonal superstructure with a lattice constant of several nm.[13,19,20,25] However, we find large terraces separated by the Au(111) interlayer spacing and decorated by a fine dotted pattern with no apparent order. Upon further magnification, Fig. 1(e), we can clearly discern the superstructure underneath a layer of round protrusions with about 8 Å diameter, which are typically associated with single adatoms. The adatoms sit exactly on the Eu sites of the lattice. They can also be displaced by lateral atomic manipulation with the same behavior as single adatoms.[26] In the left half of Fig. 1(e), we cleaned up all the adatoms to get a better view of the supporting surface. Here, the Eu sites are visualized as bright protrusions with $d_{\mathrm{Eu-Eu}} = 5.6$ Å. The long-range superstructure is commensurate with periodicity $d_r = 9.75$ Å (corresponding to precisely the observed LEED pattern). The resulting lattice parameter of the Au matrix in which the Eu atoms are embedded is $d_{\mathrm{Au}} = d_{\mathrm{Eu}}/\sqrt{3} = 3.25$ Å. This amounts to a 12% expansion with respect to the pristine Au(111) lattice.

Patches of this $EuAu_2$ phase (A-phase) start forming for $T_s > 210\,^{\circ}C$. The presence of the adatoms is ubiquitous in the whole $210 < T_s < 350\,^{\circ}C$ range and their density is independent of T_s. These adatoms cannot be imaged at room temperature, where most of the scans manifest just as instabilities of the tip-sample gap. If the dose is increased up to a nominal coverage of 1.4 ML of $EuAu_2$ at $T_s = 345\,^{\circ}C$, a second phase (B) starts appearing [Figs. 1(a) and 1(d)]. The B-phase exhibits an apparent height at $V_b = 10$ mV of 0.3 Å above the A-phase. Adatoms are now clustered in bigger structures and, consequently, larger areas of the $EuAu_2$ surfaces become exposed. The close-packed directions of both phases match perfectly on top of each other, and their lattice parameters cannot be distinguished within the STM accuracy. However, the B-phase displays more inhomogeneities in the STM contrast of Eu atoms. The atomically resolved image of Fig. 1(d) shows that the 9×9 reconstruction becomes distorted, and it is no longer commensurate. As will be shown below, the two phases have different magnetic behavior. The B-phase can also be induced in single A-phase samples by a longer post-annealing above the optimum T_s, see Figs. 1(c), and 1(f). It is well-known that RE atoms can be segregated from the bulk Au crystals in samples utilized for $REAu_2$ alloying, giving rise to non-stoichiometric RE-Au alloys with various geometries.[25] Therefore, the appearance of the B-phase for higher Eu doses or after an additional Eu contribution during the post-annealing suggests that

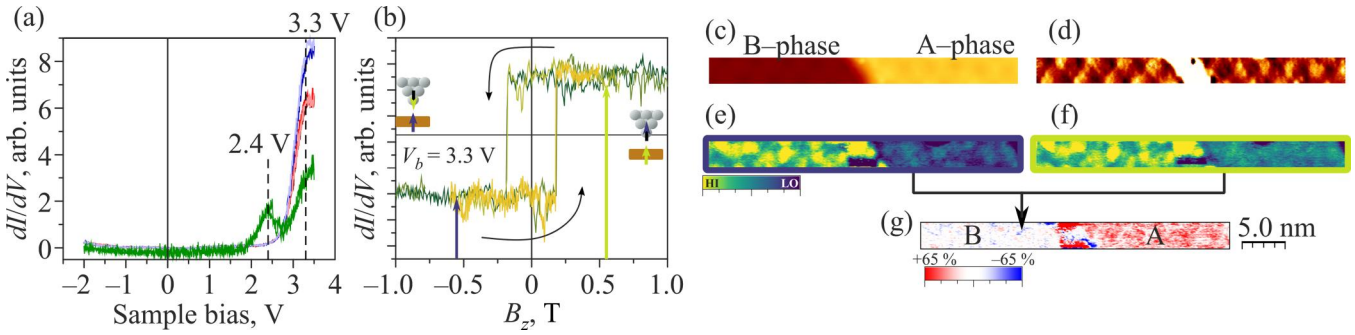

FIG. 2. Spin-polarized characterization of $EuAu_2$. (a) Point spectroscopy taken at the positions indicated by colour-coded stars in Fig. 1(e). (b) Spin sensitive *dI*/*dV* intensity of the A-phase region in (c) taken at $V_b = 3.3$ V as a function of the magnetic field normal to the surface. (c), (d) Topography and differentiated topography, respectively of the region free of Eu adatoms selected for SP-STM measurements. (e), (f) *dI*/*dV* maps of the A- and B-phases taken with antiparallel (– 0.6 T) and parallel (+ 0.6 T) tip-sample magnetizations, respectively. The magnetic state for each one is indicated by arrows and cartoons in (b). (g) Spin contrast map calculated as the ratio between the difference between (f) and (e) over the average A-phase *dI*/*dV* conductance. STM parameters: $V_{mod} = 10$ mV; (a) regulation set-point is 2 V/30 pA; (b) *dI*/*dV* signal taken at 3.3 V/30 pA; (c), (d) V_s/I_s is 1 V/30 pA; (e), (f) 3.3 V/30 pA. $T = 1.1$ K.

it could be a non-stoichiometric form richer in Eu than the A-phase (for instance, a bilayer).

Figure 2 shows the SP-STM study of a stripe of the $EuAu_2$ containing A- and B-phases and free of adatoms. Point spectroscopy in Fig. 2(a) shows the same unoccupied band at high positive bias previously observed in $GdAu_2$ at 2.9 V[13] but at a slightly higher $V_b = 3.3$ V. An additional resonance at $V_b = 2.4$ V appears on top of the adatoms. Magnetic field dependent *dI*/*dV* measurements taken with a bulk-Cr tip confirm that the feature at 3.3 V is spin polarized, and allow us to retrieve the local magnetization of A-phase shown in Fig. 2(b). This loop is characteristic of a relatively hard ferromagnet (coercive field of 0.18 T) with strong out-of-plane magnetic anisotropy, in agreement with spatially averaged XMCD data reported for this system.[20] As shown in the *dI*/*dV* maps for opposite magnetization directions [Figs. 2(c)–(f)] and the corresponding spin density [Fig. 2(g)], the A-phase displays a spin contrast in *dI*/*dV* of ∼28% for this Cr-tip, whereas the B-phase shows no spin polarization at all at this energy. This could be explained if the B-phase has in-plane magnetization, no spin polarization at $V_b = 3.3$ V, or it is not ferromagnetic (note that the experiment is conducted at $T = 1.1$ K).

4. ON-SURFACE SYNTHESIS OF CHIRAL GNRs

In the notation (*m*,*n*,*w*)-GNRs, chiral graphene nanoribbons have their longitudinal axis along a vector (*m*,*n*) of the graphene lattice, and enclose *w* C–C pairs in between both edges. We synthesized (3,2,8)-GNRs on $EuAu_2$ in a two-step reaction depicted in Fig. 3(a). The starting $EuAu_2$ is shown in Fig. 3(c), where most of the imaged region corresponds to the well-ordered A-phase with high adatom density, and just a narrow stripe on the top corresponds to the B-phase. Deposition of precursor 1 with the substrate at room temperature (RT) results in some structures of 4 Å in height and the disappearance of all the Eu adatoms [Fig. 3(d)]. The rough three-dimensional structure of the molecules is reminiscent of the status of anthracene-based precursors like 1 before the cyclo-dehydrogenation process.[13,15] However, contrary to the scenario in Au or $GdAu_2$, the molecular assemblies do not adopt any defined geometry, such as, for instance, self-assembled chains or wider elongated structures.

Upon annealing at 210 °C, we observe individual structures of size compatible with planarized precursors, and a few dimers not yet planarized [Fig. 3(e)]. The Eu adatoms (red arrows) reappear, as well as some other smaller adatoms (blue arrows). By annealing at 305 °C [Fig. 3(f)] all molecular structures become planar, and fused GNRs up to three precursor units (PU) in length can be distinguished, but mainly in regions with lower atom density associated with phase B (enclosed by the black rectangle). Finally, at 365 °C [Fig. 3(g)], no organic material remains on the A-phase, while just a few planarized monomers and GNRs are fused in random directions other than the designated one shown in Fig. 3(a). The small atoms marked with blue arrows persist at this temperature. At a temperature of 430 °C (not shown), all molecules and the small adatoms are desorbed from both phases, leaving the $EuAu_2$ surface as in the pre-deposition stage of Fig. 3(c).

The evolution of the OSS process upon annealing can be rationalized as follows. At low temperatures (around RT), the Eu adatoms coordinate to the pristine precursors through the Br group, although this bond is not directional, and a large variety of structures are formed. Increasing the temperature ($\sim 200\,^{\circ}C$) cleaves the carbon-bromine bonds and the precursors become fully H-passivated, releasing in this way the Eu coordination atoms and the Br leftovers (that are desorbed later on at $T > 400\,^{\circ}C$). At this temperature, Ullmann coupling of just two or three units takes place, and there are still some three-dimensional precursors. Complete cyclo-dehydrogenation is achieved at $T = 305\,^{\circ}C$. However, the presence of the adatoms clearly impedes the formation of GNR structures longer than three PU [see Fig. 3(f)], and this is more favourable in the B-phase, which offers a larger surface area for the diffusion of the precursors. As a comparison, we studied the effect of this annealing after

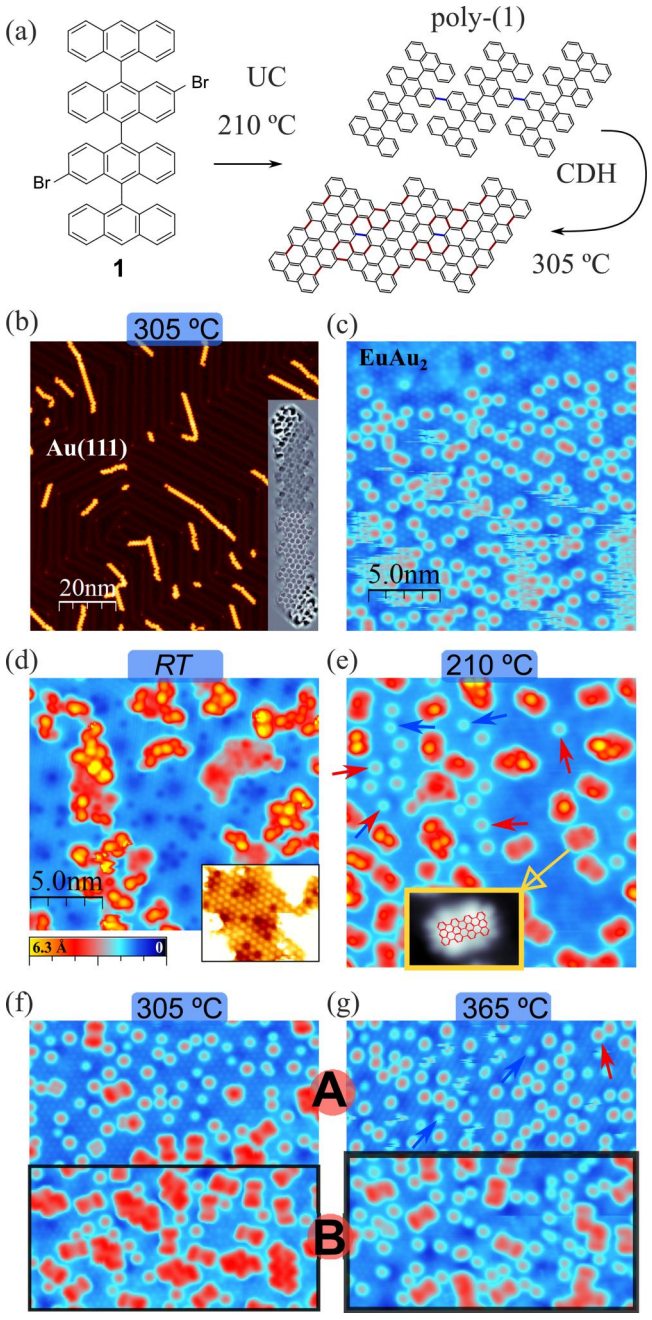

FIG. 3. Synthesis of (3,2,8)-GNRs on $EuAu_2$ monolayer. (a) Reaction scheme of precursor one leading to (3,2,8)-GNRs via Ullmann coupling (UC) and subsequent cyclo-dehydrogenation (CDH). (b) Resulting OSS of the same precursors on Au(111), the inset shows a bond resolved image of an 8 PU long (3,2,8)-GNR, taken with a functionalized CO-tip. (c) Starting $EuAu_2$ surface [prepared as in Fig. 1(b)]. (d), (e), (f), (g) Evolution of surface in (c) after depositing the same precursor dose as in (b) for different post-annealing temperatures between RT and 365 °C. STM parameters: (b), (d) $V_s = -0.5$ V, inset of (b) is a constant height scan at $V_b = 10$ mV; (c), (e), (f), (g) are taken at $V_s = 10$ mV. $T = 4.3$ K.

deposition of the same precursor dose on conventional Au(111). Here, high-quality (3,2,8)-GNRs are formed with lengths up to 20–30 PUs [Fig. 3(b)]. On $EuAu_2$, when the de-halogenation becomes complete, the adatoms prevent the precursors from finding each other and forming long polymeric chains. After that, it is very unlikely to form longer structures by fusing carbon atoms passivated by H-bonds in the right position. Consequently, higher annealing temperatures only contribute to creating structures with undefined geometry and, ultimately, to the complete desorption of organic material.

5. FRONTIER STATES OF CHIRAL GNRs ON $EuAu_2$

Using dI/dV tunneling spectroscopy, we obtain experimentally the spatially resolved LDOS and its energy dependence around the Fermi level for a (3,2,8)-GNR on the A-phase with a length of 3 PU, shown in Figs. 4(a) and 4(b). We find two clear resonances at −180 and 425 mV in point spectroscopy onto both the armchair termini (green and blue curves) and the chiral longitudinal edge (yellow curve). At the termini, a weak shoulder at 70 mV can also be appreciated. We map these spectroscopic features to identify the molecular orbitals they stem from. The comparison of our dI/dV maps to the theoretically simulated TB LDOS slices of the same GNR structure is displayed in Figs. 4(b) and 4(c). We do not include electron correlations in our simulation. Within this approximation, in the charge-neutral case at half filling, the SPTES that appear at the boundary between the GNR and the vacuum owing to its non-trivial topology[12] are pinned at the Fermi level. Consequently, our simulated SPTES lies very close to the Fermi level. The resemblance of the map of the resonance at −180 mV on $EuAu_2$ [Fig 4(b)] and the theoretical TB SPTES LDOS is evident. Therefore, we conclude that the SPTES is fully occupied in the GNR on $EuAu_2$. The SPTES can host up to four electrons. Since in the charge neutral gas phase state, the two SPTES (one at each side of the ribbon) are singly occupied, the fact that they are fully occupied on $EuAu_2$ implies that, at least, a charge equivalent to two electrons has been transferred from the supporting surface.

One straightforward consequence of the full occupation of the SPTES state is that they lose their magnetic open-shell character in the charge-neutral specimen. We cannot discard that higher energy states closer to the Fermi level may show magnetic instabilities in the presence of electronic correlations. This scenario would be more plausible for longer ribbons with lower energy spacing between molecular orbitals,[13] which cannot be synthesized on this surface owing to the Eu adatoms (see Sec. 4).

On the other hand, the map at 425 mV [top panel Fig. 4(b)] reproduces the spatial distribution along the chiral edge of the second eigenstate above the SPTES [thus termed the 2nd molecular orbital (MO) in Fig. 4(c)], characterized by one nodal point and two maxima. The weak feature at 70 mV, however, does not match the simulated 1st MO well. We attribute this partial disagreement to our simplified model without electron correlations. A correlation gap for the edge state of 10 meV has been demonstrated in long (3,1,8)-GNRs on $GdAu_2$,[13] which can get as large as 100 meV on top of insulating surfaces.[14] In our case, we expect a sizable impact of electron correlations for two reasons: (i) The

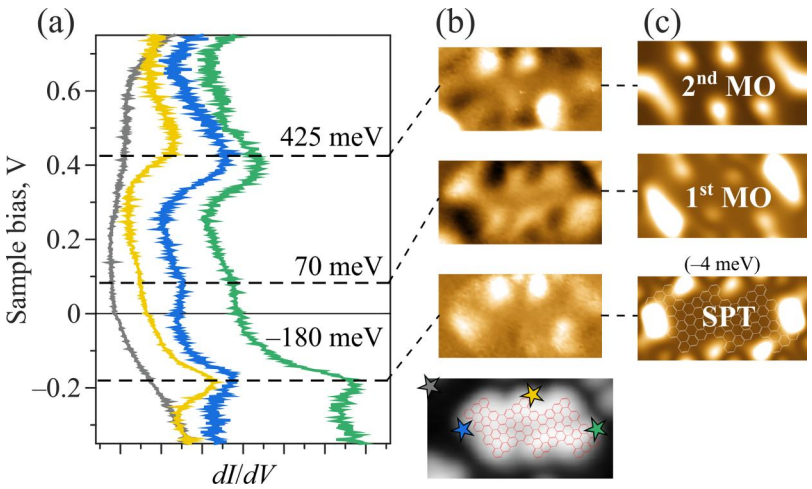

FIG. 4. Study of the frontier states of (3,2,8)-GNR on the A-phase of $EuAu_2$/Au(111). (a) Selected *dI/dV* spectroscopy curves acquired at the positions marked by stars in (b). (b) Constant current *dI/dV* maps on $EuAu_2$ of the resonances identified by dashed lines in (a) at V_b = 425 mV, 70 mV, and −180 mV. The bottom panel shows a schematic representation of the GNR superimposed to a STM topography image. (c) Simulated tight-binding (TB, see Sec. 2) images of the SPTES (see text) state and the next two eigen-states of the GNR. STM parameters: *dI/dV* spectroscopy regulation in (a), (b), and (c) is $V_s/I_s = -0.5$ V/300 pA , and V_{mod} = 10 mV. T = 4.3 K. Post annealing temperature for OSS is $T_s = 307$ °C.

GNR is very short, and thus the wave function is more spatially confined; and (ii) (3,2,8)-GNRs have a more robust non-trivial topological state than their (3,1,8) counterparts.[12] Altogether, this can give rise to a strong renormalization of the eigenenergies and a mixing of the different molecular orbitals obtained in the absence of electron-electron interactions.

6. CONCLUSIONS

We show that graphene nanoribbons can be synthesized on the $EuAu_2$ surface by Ullmann coupling and subsequent cyclo-dehydrogenation.[13] However, we find that $EuAu_2$/Au(111) exhibits randomly dispersed Eu adatoms that stabilize the surface, and that this is an intrinsic feature of the epitaxial overlayer. These adatoms proved to be detrimental to Ullmann coupling, leading to very short GNRs and preventing the formation of long GNRs with arbitrary lengths. Despite this impediment, $EuAu_2$ can be included in the toolbox of magnetic rare-earth Au alloys compatible with OSS of GNRs, together with the previously reported cases of $GdAu_2$[13,17] and $TbAu_2$.[16] While the latter substrates were reported to produce very weak *n*-doping (0.1 e^-/nm), the case of $EuAu_2$ seems to induce a more pronounced charge transfer (0.5 e^-/nm), driving the charge neutrality point of the (3,2,8)-GNR with 3 PU down to –180 meV.

The surface of $EuAu_2$ exhibits a strong spin polarization at 3.3 eV above the Fermi level, accounting for its ferromagnetic character with out-of-plane magnetocrystalline anisotropy. Although the short length of the GNRs prevents us from drawing definitive conclusions on their magnetic coupling, the combination of a spin-polarized surface with its capability to catalyze Ullmann coupling and cyclo-dehydrogenation makes $EuAu_2$ an excellent platform for studying how finite π-conjugated systems interact with nearby spin moments.

ACKNOWLEDGMENTS

The authors gratefully acknowledge financial support from the Spanish MICIU/AEI/10.13039/501100011033 and by "ERDF A way of making Europe" through grant PID2022–138750NB-C21 (D.S., F.L.T, J.L.C.), as well as from the Excellence Program Severo Ochoa CEX2023–001286-S. This work has also been supported by the Aragon Government (E13–23R and E12–23R grants).

REFERENCES

[1]S. Song, J. Su, M. Telychko, J. Li, G. Li, Y. Li, C. Su, J. Wu, and J. Lu, "On-surface synthesis of graphene nanostructures with p-magnetism," Chem. Soc. Rev. **50**, 3238 (2021).
[2]D. G. de Oteyza and T. Frederiksen, "Carbon-based nanostructures as a versatile platform for tunable π-magnetism," J. Phys. Cond. Matter **34**, 443001 (2022).
[3]M. Corso, E. Carbonell-Sanromà, and D. G. de Oteyza, "Bottom-Up fabrication of atomically precise graphene nanoribbons," in *On Surface Synthesis II*, Advances in Atom and Single Molecule Machines, edited by Dimas G. de Oteyza and Celia Rogero (Springer International Publishing, Cham, 2018), p. 113.
[4]V. Saraswat and R. M. Jacobberger, and M. S. Arnold, "Materials science challenges to graphene nanoribbon electronics," ACS Nano **15**, 3674 (2021).
[5]J. Zhang, O. Braun, G. B. Barin, S. Sangtarash, J. Overbeck, R. Darawish, M. Stiefel, R. Furrer, A. Olziersky, K. Müllen, I. Shorubalko, A. H. S. Daaoub, P. Ruffieux, R. Fasel, and H. Sadeghi, M. L. Perrin, and M. Calame, "Tunable quantum dots from atomically precise graphene nanoribbons using a multigate architecture," Adv. Electronic Mater. **9**, 2201204 (2023).
[6]J. P. Llinas, A. Fairbrother, G. B. Barin, W. Shi, K. Lee, S. Wu, B. Y. Choi, R. Braganza, J. Lear, N. Kau, W. Choi, C. Chen, Z. Pedramrazi, T. Dumslaff, A. Narita, X. Feng, K. Müllen, F. Fischer, A. Zettl, P. Ruffieux, E. Yablonovitch, M. Crommie, R. Fasel, and J. Bokor, "Short-channel field-effect transistors with 9-atom and 13-atom wide graphene nanoribbons," Nature Commun. **8**, 633 (2017).
[7]S. Clair and D. G. de Oteyza, "Controlling a chemical coupling reaction on a surface: Tools and strategies for on-surface synthesis," Chem. Rev. **119**, 4717 (2019).
[8]O. V. Yazyev, R. B. Capaz, and S. G. Louie, "Theory of magnetic edge states in chiral graphene nanoribbons," Phys. Rev. B **84**, 115406 (2011).
[9]S. Wang, L. Talirz, C. A. Pignedoli, X. Feng, K. Müllen, R. Fasel, and P. Ruffieux, "Giant edge state splitting at atomically precise graphene zigzag edges," Nature Commun. **7**, 11507 (2016).
[10]P. Ruffieux, S. Wang, B. Yang, C. Sánchez-Sánchez, J. Liu, T. Dienel, L. Talirz, P. Shinde, C. A. Pignedoli, D. Passerone, T. Dumslaff, X. Feng,

K. Müllen, and R. Fasel, "Onsurface synthesis of graphene nanoribbons with zigzag edge topology," Nature **531**, 489 (2016).
[11]N. Merino-Díez, J. Li, A. GarciaLekue, G. Vasseur, M. Vilas-Varela, E. Carbonell-Sanromà, M. Corso, J. Enrique Ortega, D. Peña, and J. I. Pascual, and D. G. de Oteyza, "Unraveling the electronic structure of narrow atomically precise chiral graphene nanoribbons," J. Phys. Chem. Lett. **9**, 25 (2018).
[12]J. Li, S. Sanz, N. Merino-Díez, M. Vilas-Varela, A. Garcia-Lekue, M. Corso, D. G. de Oteyza, T. Frederiksen, and D. Peña, and J. I. Pascual, "Topological phase transition in chiral graphene nanoribbons: From edge bands to end states," Nature Commun. **12**, 5538 (2021).
[13]J. Brede, N. Merino-Díez, A. Berdonces-Layunta, S. Sanz, A. Domínguez-Celorrio, J. Lobo-Checa, M. Vilas-Varela, D. Peña, T. Frederiksen, J. I. Pascual, D. G. de Oteyza, and D. Serrate, "Detecting the spin-polarization of edge states in graphene nanoribbons," Nature Commun. **14**, 6677 (2023).
[14]A. Domínguez-Celorrio, L. Edens, S. Sanz, M. Vilas-Varela, J. Martinez-Castro, D. Peña, V. Langlais, T. Frederiksen, J. I. Pascual, and D. Serrate, "Systematic modulation of charge and spin in graphene nanoribbons on MgO," Nature Commun. **16**, 5632 (2025).
[15]J. Cai, P. Ruffieux, R. Jaafar, M. Bieri, T. Braun, S. Blankenburg, M. Muoth, A. P. Seitsonen, M. Saleh, X. Feng, K. Müllen, and R. Fasel, "Atomically precise bottom-up fabrication of graphene nanoribbons," Nature **466**, 470–473 (2010).
[16]Y. Que, B. Liu, Y. Zhuang, C. Xu, K. Wang, and X. Xiao, "Onsurface synthesis of graphene nanoribbons on twodimensional rare earth–gold intermetallic compounds," J. Phys. Chem. Lett. **11**, 5044 (2020).
[17]L. Edens, F. Romero-Lara, T. Sai, K. Biswas, M. Vilas-Varela, T. Frederiksen, D. Peña, F. Schulz, and J. I. Pascual, Adv. Mater., e10753 (2025).
[18]M. Bazarnik, M. Abadia, J. Brede, M. Hermanowicz, E. Sierda, M. Elsebach, T. Hänke, and R. Wiesendanger, "Atomically resolved magnetic structure of a GD-Au surface alloy," Phys. Rev. B **99**, 174419 (2019).
[19]L. Fernandez, M. Blanco-Rey, R. CastrilloBodero, M. Ilyn, K. Ali, E. Turco, M. Corso, M. Ormaza, P. Gargiani, M. A. Valbuena, A. Mugarza, P. Moras, P. M. Sheverdyaeva, A. K. Kundu, M. Jugovac, C. Laubschat, J. E. Ortega, and F. Schiller, "Influence of 4f filling on electronic and magnetic properties of rare earthau surface compounds," Nanoscale **12**, 22258 (2020).
[20]M. Blanco-Rey, R. Castrillo-Bodero, K. Ali, P. Gargiani, F. Bertran, P. M. Sheverdyaeva, J. E. Ortega, L. Fernandez, and F. Schiller, "Effect of the valence state on the band magnetocrystalline anisotropy in two-dimensional rare-earth/noblemetal compounds," Phys. Rev. Res. **4**, 013237 (2022).
[21]N. Bassi, J. Wilhelm, N. Krane, F. Xiang, P. Čmelová, E. Turco, P. Gargiani, C. A. Pignedoli, M. Juríček, R. Fasel, R. Korytár, and P. Ruffieux, "Proximity-driven magnetic coupling between an open-shell nanographene and a rare-earth surface alloy," ACS Nano **19**, 33868 (2025).
[22]Y. Hancock, A. Uppstu, K. Saloriutta, A. Harju, and M. J. Puska, "Generalized tight-binding transport model for graphene nanoribbon-based systems," Phys. Rev. B: Cond. Matter Mater. Phys. **81**, 3 (2010).
[23]S. S. Wuhl, N. Papior, M. Brandbyge, and T. Frederiksen, hubbard v0.4.2, (2023).
[24]Nick Papior and Pol Febrer Calabozo. sisl v0.16.2 (2025).
[25]M. Corso, L. Fernández, F. Schiller, and J. E. Ortega, "Au(111)based nanotemplates by gd alloying," ACS Nano **4**, 1603 (2010).
[26]M. Moro-Lagares, J. Fernández, P. Roura-Bas, M. R. Ibarra, A. A. Aligia, and D. Serrate, "Quantifying the leading role of the surface state in the kondo effect of Co/Ag(111)," Phys. Rev. B **97**, 235442 (2018).